Publisher: GSA
Journal: GEOL: Geology
DOI:10.1130/G38795.1

Seismic imaging of magma sills beneath an ultramafic-hosted hydrothermal system

J. Pablo Canales[1], Robert A. Dunn[2], Ryuta Arai[3], and Robert A. Sohn[1]

[1]*Department of Geology and Geophysics, Woods Hole Oceanographic Institution, Woods Hole, Massachusetts 02543, USA*

[2]*Department of Geology and Geophysics, University of Hawaii at Manoa, Hawaii 96822, USA*

[3]*Research and Development Center for Earthquake and Tsunami, Japan Agency for Marine-Earth Science and Technology, Yokohama, Kanagawa, Japan*

ABSTRACT

Hydrothermal circulation at mid-ocean ridge volcanic segments extracts heat from crustal magma bodies. However, the heat source driving hydrothermal circulation in ultramafic outcrops, where mantle rocks are exhumed in low-magma supply environments, has remained enigmatic. Here we use a three-dimensional *P*-wave velocity model derived from active-source wide-angle refraction/reflection ocean bottom seismometer data and pre-stack depth-migrated images derived from multichannel seismic reflection data to investigate the internal structure of the Rainbow ultramafic massif, which is located in a non-transform discontinuity of the Mid-Atlantic Ridge. Seismic imaging reveals that the ultramafic rocks composing the Rainbow massif have been intruded by a large number of magmatic sills, distributed throughout the massif at depths of ~2–10 km. These sills, which appear to be at varying stages of crystallization, can supply the heat needed to drive high-temperature hydrothermal circulation, and thus

Publisher: GSA
Journal: GEOL: Geology
DOI:10.1130/G38795.1

provide an explanation for the hydrothermal discharge observed in this ultramafic setting. Our results demonstrate that high-temperature hydrothermal systems can be driven by heat from deep-sourced magma even in exhumed ultramafic lithosphere with very low magma supply.

INTRODUCTION

Exposures of mantle rocks are common along mid-ocean ridges spreading at slow to ultraslow rates (<55 mm/yr), especially in magma poor regions (e.g., Tucholke and Lin, 1994). Hydrothermal circulation at these sites produces serpentine via the reaction of seawater with ultramafic rocks (e.g., Allen and Seyfried, 2004), resulting in fluids enriched in H_2, CH_4, and other abiogenic hydrocarbons (e.g., Holm and Charlou, 2001). Where exit-fluid temperatures are low (<100 °C), hydrothermal circulation can be sustained by a combination of exothermic serpentinization and heat mined from hot lithosphere (e.g., Allen and Seyfried, 2004). However, a magmatic heat source is required to explain hydrothermal circulation at ultramafic sites where fluids exit the seafloor at high flow rates and elevated temperatures (>340 °C) and are enriched in CO_2 (Allen and Seyfried, 2004), despite these systems being located in settings away from neo-volcanic zones such as ridge-axis discontinuities (German et al., 1996), rift valley walls (e.g., Ondreas et al., 2012), and inside-corner highs (Okino et al., 2015). While magma systems beneath volcanic-hosted hydrothermal sites are well characterized (e.g., Singh et al., 1999), the heat sources that drive high-temperature hydrothermal systems in ultramafic settings have yet to be imaged. As a result, we have no *in situ* constraints on the geometry of the sub-surface circulation system, and an incomplete understanding of the relationship

between lithospheric accretion, extension and hydrothermal processes in ultramafic environments.

GEOLOGICAL SETTING

The Rainbow ultramafic massif is thought to be an oceanic core complex (OCC) formed by detachment faulting (Andreani et al., 2014) within a non-transform discontinuity (NTD) of the Mid-Atlantic Ridge (MAR, Fig. 1). The massif hosts the Rainbow hydrothermal field (RHF) (German et al., 1996), which vents fluids enriched in CH_4, H_2 and Fe (diagnostic of serpentinization (Holm and Charlou, 2001)) at high temperatures and flow rates (German et al., 2010), indicating that a magmatic heat source is present (Allen and Seyfried, 2004). However, the tectonized setting of the NTD lacks significant volcanic features (Andreani et al., 2014; Eason et al., 2016; Paulatto et al., 2015). The massif is largely covered by pelagic sediments, but basement outcrops expose predominately serpentinites, with sparse occurrence of plutonic rocks and basalts (Andreani et al., 2014). The presence of two inactive hydrothermal sites (Ghost City and Clamstone, Fig. 1B) is inferred from fossil evidence (Lartaud et al., 2010; Lartaud et al., 2011), but neither of them shows evidence of past high-temperature activity (Andreani et al., 2014).

NEW GEOPHYSICAL DATA AND METHODS

To understand how magmatic and tectonic processes give rise to high-temperature hydrothermal activity in an ultramafic setting we conducted a geophysical investigation of the Rainbow NTD and neighboring segments using shipboard acoustic and potential fields (Paulatto et al., 2015; Eason et al., 2016), and active-source seismic imaging. We used travel times of *P*-waves recorded by 43 ocean bottom seismometers (OBSs) (Fig.

1A) using an iterative technique to compute the three-dimensional (3-D) *P*-wave velocity (*V*p) structure (Dunn et al., 2005). The 3D tomography model was used to depth-migrate 2-D multichannel seismic (MCS) reflection data collected with an 8-km-long hydrophone streamer along 21 profiles (Fig. 1). Details about the seismic modeling and processing are given in the GSA Data Repository[1].

RESULTS AND DISCUSSION

P-wave Velocity Structure

The 3D tomography model shows large *Vp* variations within the study area (Fig. 2A, B). The Rainbow massif is underlain by a cone-shaped core of high-*Vp* mantle material that is elongated in the northeast-southwest direction (Fig. 2A, C). Above this core, the flanks of the massif and adjacent nodal basins are characterized by layers of low-to-moderately-low *Vp* (Fig. 2A, B) consistent with serpentinite or high-porosity basalts. The lower velocities on the flanks of the massif are most likely associated with highly serpentinized peridotites based on seafloor samples (Andreani et al., 2014).

Pre-Stack Depth-Migrated Images

Seismic reflection images reveal two primary types of events within the massif: reflectors beneath both flanks of the massif that dip at 35–45° away from the area where hydrothermal venting is clustered near the summit of the massif (Fig. 2D), and short, sub-horizontal reflectors broadly distributed throughout the massif confined between the northwest- and southeast-dipping reflectors (Fig. 2C, 3, 4A).

Nature of Dipping Reflectors

The dipping reflectors are associated with the boundaries between the high-*Vp* core of the massif and the overlaying lower velocity layers (Fig. 2D). This indicates that

the high-*Vp* core is separated from the overlaying layers by sharp impedance contrasts that may be produced by faulting, alteration, or lithological contacts. In cross-section the dipping reflectors resemble normal faults (Fig. 2D), but their depth extent (~5 km below seafloor, bsf below the adjacent nodal basin in some instances, Fig. 2D) would require the presence of exposed faults scarps on both flanks of the massif with kilometer-scale vertical throws. Because such scarps are not observed (Andreani et al., 2014; Paulatto et al., 2015), the dipping reflectors most likely represent lithological contacts, serpentinization fronts, or a combination of both. The cone-shaped high-*V*p core forms an inverted funnel that shoals beneath the southwest flank near the summit of the massif where hydrothermal activity is clustered (Fig. 2A), indicating that hydrothermal outflow zones may be to some extent controlled by the sub-seafloor lithological and alteration structure.

Magma Sills Driving Ultramafic-Hosted Hydrothermal Circulation

The sub-horizontal reflectors occupy an area of ~4.6 km x 8 km (Fig. 1B, 4A), and are distributed within a depth range from ~2–10 km bsf (the majority being at 3–6 km bsf, Fig. 4B). Their appearance and geometry are very similar to that of melt lenses imaged in young crust at other spreading centers (e.g., Marjanović et al., 2014; Nedimović et al., 2005), leading to the conclusion that they represent magmatic sills. The majority of them intrude material with *V*p>7.5 km/s; this implies an ultramafic nature with little or no alteration due to serpentinization (<15%, Fig. 4C). Only a few sills are imaged within material with *V*p = 6.8–7.3 km/s, which could either correspond to 20–40% serpentinite, gabbros, or a mixture of both (Fig. 4C).

Publisher: GSA
Journal: GEOL: Geology
DOI:10.1130/G38795.1

Our 3D *Vp* model does not have the resolution to resolve the small-scale structure of individual sills. However, the sills located closer to the RHF are, in general, of larger dimensions and have larger reflection amplitudes (relative to surrounding reflectivity) than those located farther away (Fig. 3). This, and the high temperature of the RHF fluids, thus suggests that the sills located beneath the vent field are most likely partially molten intrusions that provide the heat to drive hydrothermal circulation, while the rest of the sills are likely solidified. Our MCS data can image both partially molten and solidified intrusions because they are emplaced within a high *Vp* matrix, and thus generate a negative impedance contrast with their host rock (Fig. 2C, 4A, D). The presence of low-*Vp* sills may result in underestimation of the tomographically derived background *Vp*, but we quantify this effect to be no more than 0.2 km/s (see the GSA Data Repository[1]).

Using previous estimates of heat flux and duration of hydrothermal activity at the RHF (see the GSA Data Repository[1]), we find that the heat delivered by solidification of the imaged sills could cumulatively support high-temperature hydrothermal circulation for a period of ~1,600-3,000 years, which is ~7–30% of the total hydrothermal system lifespan (Cave et al., 2002; Kuznetsov et al., 2006). These estimates approximately double if additional heat released by crystallization of melt impregnating peridotites that is not accounted for in the seismically imaged sills is factored in (Table DR3). By comparison, high-temperature discharge at the longer-lived, volcanic-hosted TAG active hydrothermal field has been estimated to occur during only 1–2% of the system lifespan (Humphris and Cann, 2000). Our results thus suggest that the RHF has a greater time-averaged rate of hydrothermal discharge than the TAG field, which may explain why the

massive sulfide deposits at the RHF have structural and mineralogical characteristics comparable to those of the TAG field (Marques et al., 2007) despite being a younger system.

Sill Intrusions in the Upper Mantle at NTDs

The lateral dimensions of the sills (a few hundred meters up to ~1,400 m in length, with the majority being 200–400 m long, Fig. 4C) and the ultramafic nature of the host rock that they intrude presents a scenario similar to the Moho transition zone in ophiolites, where gabbroic sills that are tens to hundreds of meters long and 0.1-100 m thick intrude ultramafic host rock (Boudier et al., 1996; Kelemen and Aharonov, 1998). Small gabbroic bodies intruding ultramafic outcrops are also observed along other portions of the MAR (e.g., Dick et al., 2008), and if emplacement is rapid enough and sustained over sufficiently long periods of time then thick gabbroic crustal sections may be accreted (Grimes et al., 2008). At the Rainbow massif, however, the sills we image occupy 4.8-9.2 km^3 (assuming a sill thickness of 80-150 m), which is only 1-2% of the volume of the exhumed ultramafic material (defined as material at depths less than 8 km bsf and with Vp>7.3 km/s). This suggests that sill emplacement at the Rainbow massif is slow compared to OCCs with large gabbroic cores (e.g., Grimes et al., 2008), perhaps because of its location within an axial discontinuity.

Exhumation of OCCs involves flexural rotation of the detachment footwall (Garcés and Gee, 2007). Our observation of sub-horizontal sills at the Rainbow massif thus implies that if the massif was exhumed along a detachment fault in a manner similar to that of other OCCs (Andreani et al., 2014), then the sills must have been emplaced after, or at the very end of, footwall rotation and exhumation. This interpretation is

consistent with the idea that exhumation of an OCC is terminated by magma emplacement into the footwall (MacLeod et al., 2009). Alternatively, if sill emplacement has occurred throughout the formation of the Rainbow massif, our observations indicate that the massif has not been significantly rotated during exhumation. This scenario could be possible if the massif was exhumed due to buoyancy forces resulting from the volume increase associated with serpentinization (O'Hanley, 1992). The tectonic setting of the Rainbow massif, being located within a NTD, could result in different deformation and exhumation mechanisms compared to OCCs formed at segment centers or inside corners, but we do not currently have enough information to address this hypothesis.

Our experiment did not resolve a potential low-*Vp* source region for the magmatic sills that intrude the massif, a region that is commonly observed beneath volcanic spreading segments (Dunn et al., 2000). The source region for the sills must thus either lie deeper than the region that our seismic tomography experiment can resolve (>8 km bsf), or be located within the neighboring spreading segments (German and Parson, 1998), rthus equiring lateral magma propagation. The lack of a volcanic magnetization signature on the massif (Paulatto et al., 2015) argues against lateral emplacement of the sills, as do the sill depths (~3-6 km bsf), because dikes propagating laterally from a segment center into a NTD are predicted to shoal towards the segment end and breach the seafloor (Behn et al., 2006). The high-magnetization volcanic cones and ridges located at the ends of the neighboring segments (Paulatto et al., 2015) (Fig. 1B) probably mark the loci of maximum dike propagation along these segments. The most plausible magma source region is thus directly beneath the massif, with melt migrating vertically through the upper mantle into the NTD. Our results thus provide compelling evidence that deep-

sourced magma can intrude exhumed ultramafic lithosphere to drive hydrothermal circulation even in highly-tectonized regions with low, long-term magma supply.

ACKNOWLEDGMENTS

This research was funded by National Science Foundation (NSF) grants OCE-0961680 and OCE-0961151. We thank the RV *M.G. Langseth*'s Captain, crew, and technical staff, and the NSF-funded Ocean Bottom Seismograph Instrument Pool (OBSIP, http://www.obsip.org) managers and technical staff for their efforts, which made possible the success of cruise MGL1305. OBSIP data are archived at the IRIS Data Management Center (Incorporated Research Institutions for Seismology; http://www.iris.edu).

REFERENCES CITED

Allen, D.E., and Seyfried, W.E., 2004, Serpentinization and heat generation: constraints from Lost City and Rainbow hydrothermal systems: Geochimica et Cosmochimica Acta, v. 68, p. 1347–1354, doi:10.1016/j.gca.2003.09.003.

Andreani, M., Escartín, J., Delacour, A., Ildefonse, B., Godard, M., Dyment, J., Fallick, A.E., and Fouquet, Y., 2014, Tectonic structure, lithology, and hydrothermal signature of the Rainbow massif (Mid-Atlantic Ridge 36°14′N): Geochemistry Geophysics Geosystems, v. 15, p. 3543–3571, doi:10.1002/2014GC005269.

Behn, M.D., Buck, W.R., and Sacks, I.S., 2006, Topographic controls on dike injection in volcanic rift zones: Earth and Planetary Science Letters, v. 246, p. 188–196, doi:10.1016/j.epsl.2006.04.005.

Boudier, F., Nicolas, A., and Ildefonse, B., 1996, Magma chambers in the Oman ophiolite: fed from the top and the bottom: Earth and Planetary Science Letters, v. 144, p. 239-250, doi: 10.1016/0012-821X(96)00167-7.

Cave, R.R., German, C.R., Thomson, J., and Nesbitt, R.W., 2002, Fluxes to sediments underlying the Rainbow hydrothermal plume at 36°14′N on the Mid-Atlantic Ridge: Geochimica et Cosmochimica Acta, v. 66, p. 1905–1923, doi:10.1016/S0016-7037(02)00823-2.

Dick, H. J. B., Tivey, M. A., and Tucholke, B. E., 2008, Plutonic foundation of a slow-spread ridge segment: Oceanic core complex at Kane Megamullion, 23°30'N, 45°20'W: Geochemistry, Geophysics, Geosystems, v. 9, no. 5, p. Q05014, doi:10.1029/2007GC001645.

Dunn, R.A., Lekic, V., Detrick, R.S., and Toomey, D.R., 2005, Three-dimensional seismic structure of the Mid-Atlantic Ridge (35°N): Evidence for focused melt supply and lower crustal dike injection: Journal of Geophysical Research, v. 110, p. B09101, doi:10.1029/2004JB003473.

Dunn, R.A., Toomey, D.R., and Solomon, S.C., 2000, Three-dimensional seismic structure and physical properties of the crust and shallow mantle beneath the East Pacific Rise at 9° 30′N: Journal of Geophysical Research, v. 105, p. 23,537–23,555, doi:10.1029/2000JB900210.

Eason, D.E., Dunn, R.A., Canales, J.P., and Sohn, R., 2016, Segment-scale variations in seafloor volcanic and tectonic processes from multibeam sonar imaging, Mid-Atlantic Ridge Rainbow region (35º45′-36º35'N): Geochemistry Geophysics Geosystems, v. 17, p. 3560–3579, doi:10.1002/2016GC006433.

226 Garcés, M., and Gee, J., 2007, Paleomagnetic evidence of large footwall rotations
227 associated with low-angle faults at the Mid-Atlantic Ridge: Geology, v. 35, no. 3, p.
228 279-282, doi: 10.1130/G23165A.1.
229 German, C.R., and Parson, L.M., 1998, Distributions of hydrothermal activity along the
230 Mid-Atlantic Ridge: Interplay of magmatic and tectonic controls: Earth and
231 Planetary Science Letters, v. 160, p. 327–341, doi:10.1016/S0012-821X(98)00093-4.
232 German, C.R., Parson, L.M., and Team, H.S., 1996, Hydrothermal exploration near the
233 Azores Triple Junction: Tectonic control of venting at slow-spreading ridges: Earth
234 and Planetary Science Letters, v. 138, p. 93–104, doi:10.1016/0012-821X(95)00224-
235 Z.
236 German, C.R., Thurnherr, A.M., Knoery, J., Charlou, J.-L., Jean Baptiste, P., and
237 Edmonds, H.N., 2010, Heat, volume and chemical fluxes from submarine venting: A
238 synthesis of results from the Rainbow hydrothermal field, 36°N MAR: Deep-Sea
239 Research, v. 57, p. 518–527, doi:10.1016/j.dsr.2009.12.011.
240 Grimes, C. B., John, B. E., Cheadle, M. J., and Wooden, J. L., 2008, Protracted
241 construction of gabbroic crust at a slow spreading ridge: Constraints from $^{206}Pb/^{238}U$
242 zircon ages from Atlantis Massif and IODP Hole U1309D (30°N, MAR):
243 Geochemistry, Geophysics, Geosystems, v. 9, p. Q08012,
244 doi:08010.01029/02008GC002063.
245 Holm, N.G., and Charlou, J.L., 2001, Initial indications of abiotic formation of
246 hydrocarbons in the Rainbow ultramafic hydrothermal system, Mid-Atlantic Ridge:
247 Earth and Planetary Science Letters, v. 191, p. 1–8, doi:10.1016/S0012-
248 821X(01)00397-1.

249 Humphris, S.E., and Cann, J.R., 2000, Constraints on the energy and chemical balances
250 of the modern TAG and ancient Cyprus seafloor sulfide deposits: Journal of
251 Geophysical Research, v. 105, p. 28,477–28,488, doi:10.1029/2000JB900289.
252 Kelemen, P. B., and Aharonov, E., 1998, Periodic formation of magma fractures and
253 generation of layered gabbros in the lower crust beneath oceanic spreading ridges, *in*
254 Buck, W. R., Delaney, P. T., Karson, J. A., and Lagabrielle, Y., eds., Faulting and
255 Magmatism at Mid-Ocean Ridges, Volume 106: Washington, D.C., AGU, p. 267-
256 289, doi: 10.1029/GM106p0267.
257 Kuznetsov, V., Cherkashev, G., Lein, A., Shilov, V., Maksimov, F., Arslanov, K.,
258 Stepanova, T., Baranova, N., Chernov, S., and Tarasenko, D., 2006, ^{230}Th/U dating
259 of massive sulfides from the Logatchev and Rainbow hydrothermal fields (Mid-
260 Atlantic Ridge): Geochronometria, v. 25, p. 51–55.
261 Lartaud, F., de Rafaelis, M., Oliver, G., Krylova, E., Dyment, J., Ildefonse, B., Thibaud,
262 R., Gente, P., Hoise, E., Meistertzheim, A.-L., Fouquet, Y., Gaill, F., and Le Bris, N.,
263 2010, Fossil clams from a serpentinite-hosted sedimented vent field near the active
264 smoker complex Rainbow, MAR, 36°13′N: Insight into the biogeography of vent
265 fauna: Geochemistry, Geophysics, Geosystems, v. 11, Q0AE01,
266 doi:10.1029/2010GC003079.
267 Lartaud, F., Little, C.T.S., de Rafaelis, M., Bayon, G., Dyment, J., Ildefonse, B., Gressier,
268 V., Fouquet, Y., Gaill, F., and Le Bris, N., 2011, Fossil evidence for serpentinization
269 fluids fueling chemosynthetic assemblages: Proceedings of the National Academy of
270 Sciences of the United States of America, v. 108, p. 7698–7703,
271 doi:10.1073/pnas.1009383108.

MacLeod, C. J., Searle, R. C., Murton, B. J., Casey, J. F., Mallows, C., Unsworth, S. C., Achenbach, K. L., and Harris, M., 2009, Life cycle of oceanic core complexes: Earth and Planetary Science Letters, v. 287, no. 3-4, p. 333-344, doi:10.1016/j.epsl.2009.08.016.

Marjanović, M., Carbotte, S., Carton, H., Nedimović, M.R., Mutter, J.C., and Canales, J.P., 2014, A multi-sill magma plumbing system beneath the axis of East Pacific Rise: Nature Geoscience, v. 7, p. 825–829, doi:10.1038/ngeo2272.

Marques, A.F.A., Barriga, F.J.A.S., and Scott, S.D., 2007, Sulfide mineralization in an ultramafic-rock hosted seafloor hydrothermal system: From serpentinization to the formation of Cu–Zn–(Co)-rich massive sulfides: Marine Geology, v. 245, p. 20–39, doi:10.1016/j.margeo.2007.05.007.

Nedimović, M.R., Carbotte, S.M., Harding, A.J., Detrick, R.S., Canales, J.P., Diebold, J.B., Kent, G.M., Tischer, M., and Babcock, J., 2005, Frozen magma lenses below the oceanic crust: Nature, v. 436, p. 1149–1152, doi:10.1038/nature03944.

O'Hanley, D. S., 1992, Solution to the volume problem in serpentinization: Geology, v. 20, p. 705-708.

Okino, K., Nakamura, K., and Sato, H., 2015, Tectonic background of four hydrothermal fields along the Central Indian Ridge, *in* Ishibashi, J.-I., Okino, K., and Sunamura, M., eds., Subseafloor biosphere linked to hydrothermal systems - TAIGA Concept, Springer, Tokyo, Japan, doi:10.1007/978-4-431-54865-2_11.

Ondreas, H., Cannat, M., Fouquet, Y., and Normand, A., 2012, Geological context and vents morphology of the ultramafic-hosted Ashadze hydrothermal areas (Mid-

294 Atlantic Ridge 13°N): Geochemistry, Geophysics, Geosystems, v. 13, p. Q0AG14,
295 doi:10.1029/2012GC004433.
296 Paulatto, M., Canales, J.P., Dunn, R.A., and Sohn, R.A., 2015, Heterogeneous and
297 asymmetric crustal accretion: new constraints from multi-beam bathymetry and
298 potential field data from the Rainbow area of the Mid-Atlantic Ridge (36°15′N):
299 Geochemistry Geophysics Geosystems, v. 16, p. 2994–3014,
300 doi:10.1002/2015GC005743.
301 Singh, S.C., Collier, J.S., Harding, A.J., Kent, G.M., and Orcutt, J.A., 1999, Seismic
302 evidence for a hydrothermal layer above the solid roof of the axial magma chamber
303 at the southern East Pacific Rise: Geology, v. 27, p. 219–222, doi:10.1130/0091-
304 7613(1999)027<0219:SEFAHL>2.3.CO;2.
305 Tucholke, B. E., and Lin, J., 1994, A geological model for the structure of ridge segments
306 in slow spreading ocean crust: Journal of Geophysical Research, v. 99, p. 11,937-
307 911,958, doi: 10.1029/94JB00338.
308
309 FIGURE CAPTIONS
310
311 Figure 1. A: Regional bathymetry (Paulatto et al., 2015) and layout of the seismic
312 experiment across the Rainbow non-transform discontinuity (NTD) and neighboring
313 segments. Dashed white box shows location of maps shown in B and Figure 2A. White
314 dots—ocean bottom seismometers (OBS); MCS—multichannel seismic. Inset shows
315 location. B: Bathymetry of the Rainbow NTD. Labeled white lines are MCS profiles,
316 black segments show locations where sills have been imaged. Triangles indicate

hydrothermal sites. Closed white contours locate areas of elevated seafloor magnetization (Paulatto et al., 2015).

Figure 2. A: Shaded topography of the Rainbow non-transform discontinuity (NTD) colored according to P-wave velocity variations relative to average of the study area (black line in B) at 1 km below seafloor. Circled numbers locate the one-dimensional P-wave velocity (*V*p) profiles shown in B. Other symbols as in Figure 1B. B: Vp plotted against depth. C: Perspective views of the Rainbow massif and sub-seafloor seismic structure. Fence diagram shows sill reflectors beneath both the active Rainbow hydrothermal field (line 112) and the inactive Clamstone and Ghost City sites (line 114), highlighted in the zoomed-in panel. D: Line 110 shows prominent west- and east-dipping reflectors coincident with large lateral variations in seismic velocity. All seismic images show reflectivity overlaid on *V*p relative to average (red-blue color scale as in A). White lines show the 7.3 (~20% serpentinization) and 7.9 km/s (fresh peridotite) iso-velocity contours. V.E.—vertical exaggeration.

Figure 3. Close-up views of sub-horizontal reflectors interpreted as sills across the southwest flank (line 108), center (112), and the northeast flank of the Rainbow massif (116). Dashed line locates the Rainbow hydrothermal field (RHF). V.E.—vertical exaggeration.

Figure 4. Distribution and characteristics of sills. A: Three-dimensional distribution of sills within the Rainbow massif shown against the relative P-wave velocity (*V*p*)* along

profiles 106 and 119. Inverted triangle locates the Rainbow hydrothermal field (RHF). V.E.—vertical exaggeration. B: Histogram shows the distribution of sill depth (bsf—below seafloor). C: Histogram shows the distribution of sill length. D: *V*p and inferred degree of serpentinization at the locations of the imaged sills. Values <7.3 km/s may correspond to gabbro matrix or >20% serpentinized peridotite. Values >7.3 km/s correspond to ultramafic rocks that are <20% serpentinized.

[1]GSA Data Repository item 2017xxx, containing additional information and images about the geophysical dataset, tomography modeling and checkerboard tests, MCS processing and interpretation, and details about calculations of the energy balance of the Rainbow hydrothermal field, is available online at www.geosociety.org/pubs/ft2017.htm, or on request from editing@geosociety.org.

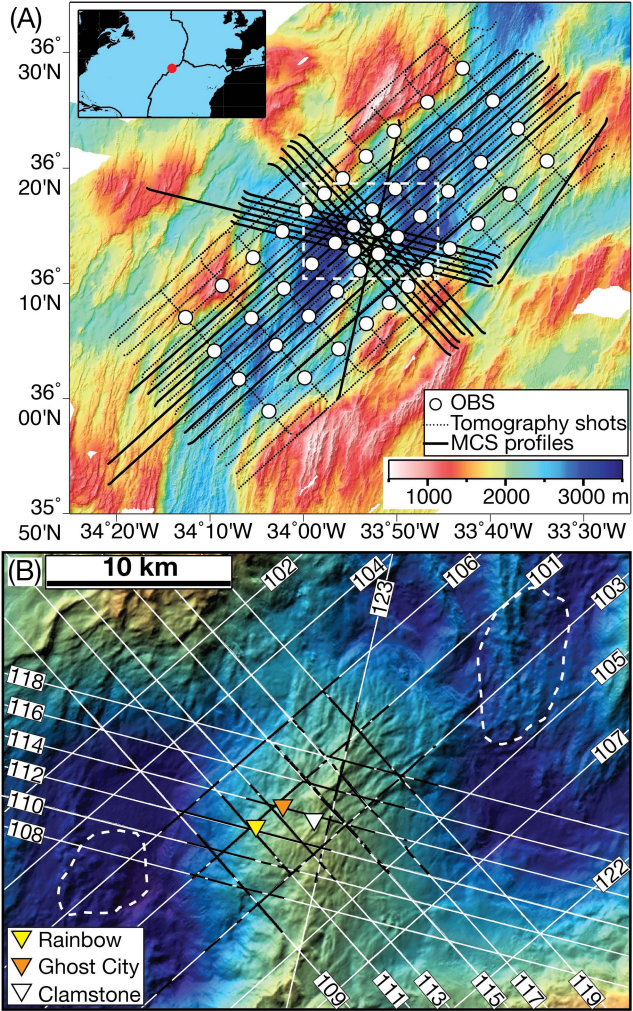
(A)
36° 30'N
36° 20'N
36° 10'N
36° 00'N
35° 50'N
34°20'W
34°10'W
34°00'W
33°50'W
33°40'W
33°30'W
OBS
Tomography shots
MCS profiles
1000
2000
3000 m
(B)
10 km
102
104
123
106
101
103
105
107
122
118
116
114
112
110
108
109
111
113
115
117
119
Rainbow
Ghost City
Clamstone

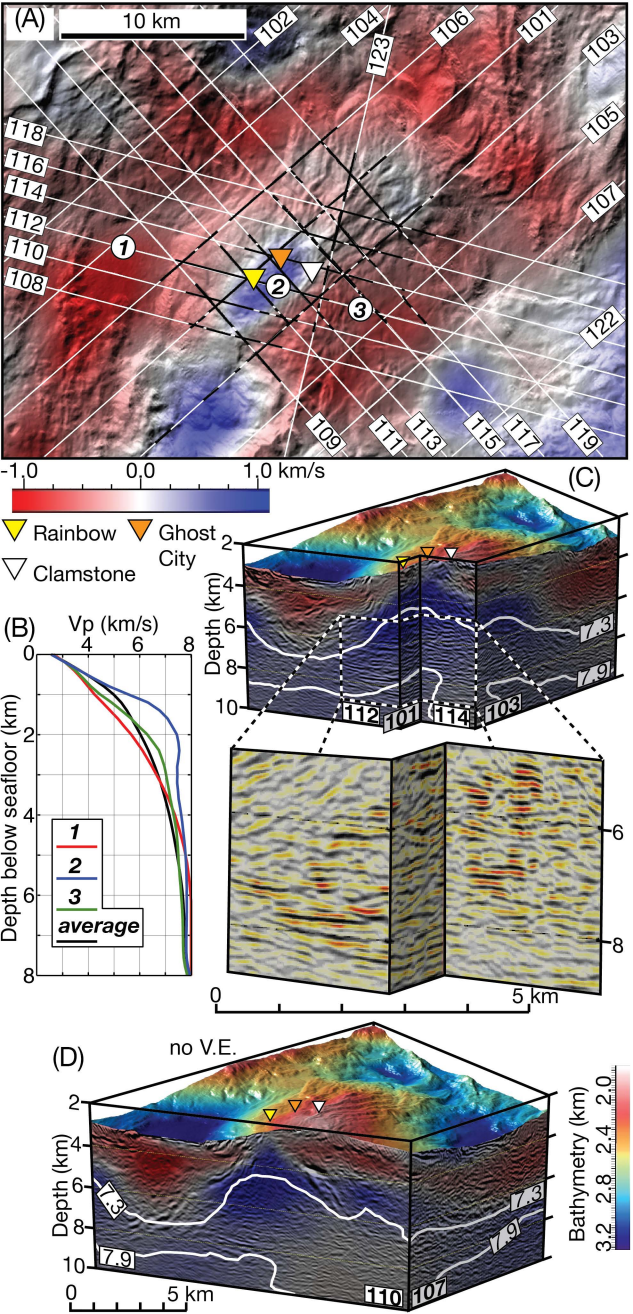
(A)
10 km
102
104
123
106
101
103
105
107
118
116
114
112
110
108
1
2
3
122
109
111
113
115
117
119
-1.0
0.0
1.0 km/s
Rainbow
Ghost City
Clamstone
(B)
Vp (km/s)
4
6
8
0
2
4
6
8
Depth below seafloor (km)
1
2
3
average
(C)
Depth (km)
2
4
6
8
10
7.3
7.9
112
101
114
103
6
8
0
5 km
(D)
no V.E.
Depth (km)
2
4
6
8
10
7.3
7.9
7.3
7.9
0
5 km
110
107
Bathymetry (km)
2.0
2.4
2.8
3.2

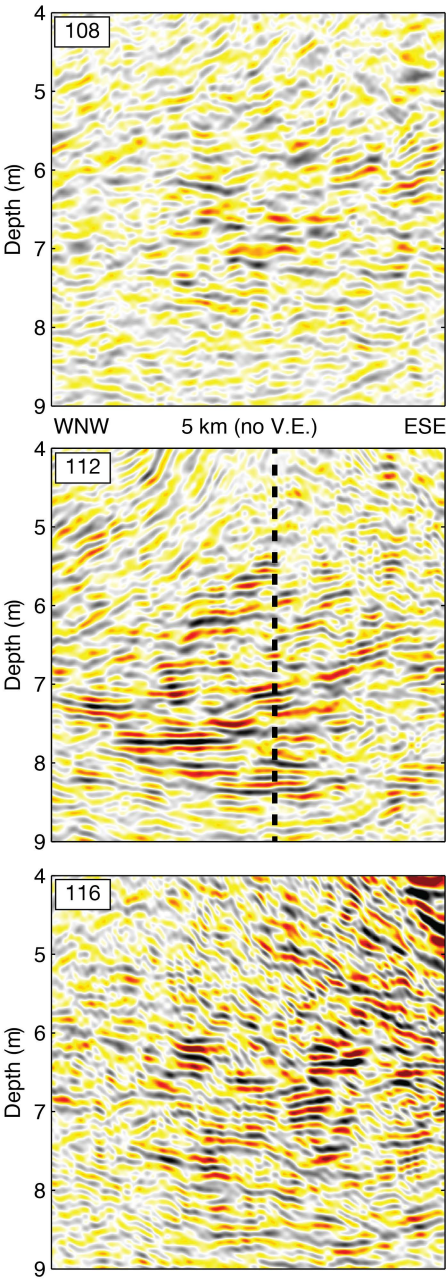
108
112
116
Depth (m)
4
5
6
7
8
9
WNW
5 km (no V.E.)
ESE

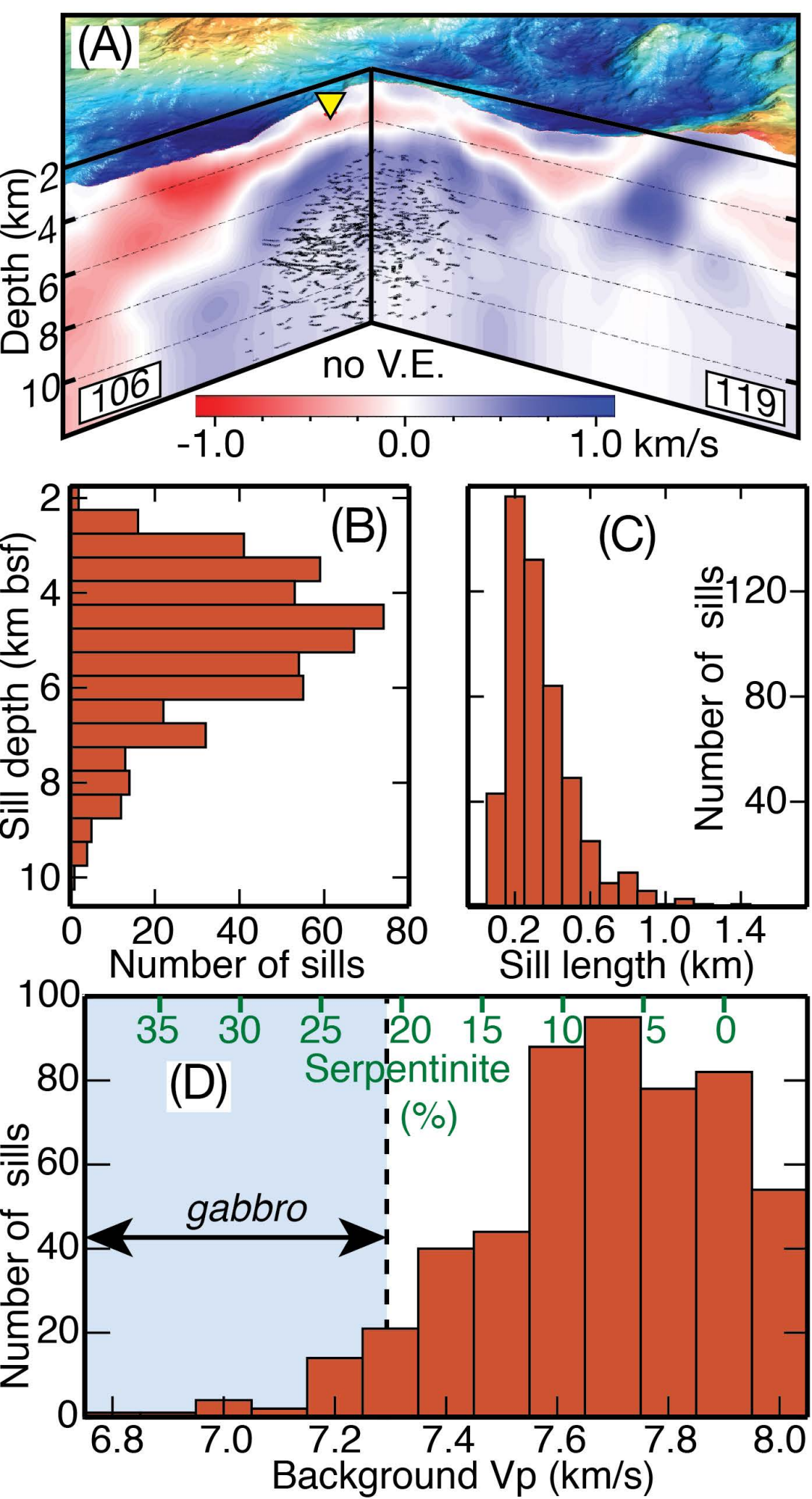
(A)
Depth (km)
2
4
6
8
10
106
no V.E.
119
-1.0
0.0
1.0 km/s
(B)
Sill depth (km bsf)
0
20
40
60
80
Number of sills
(C)
Number of sills
120
80
40
0.2
0.6
1.0
1.4
Sill length (km)
(D)
35
30
25
20
15
10
5
0
Serpentinite
(%)
gabbro
Number of sills
100
80
60
40
20
0
6.8
7.0
7.2
7.4
7.6
7.8
8.0
Background Vp (km/s)

GSA Data Repository 201Xxxx

Seismic Imaging of Magma Sills Beneath an Ultramafic-Hosted Hydrothermal System

J. Pablo Canales[1], Robert A. Dunn[2], Ryuta Arai[3], and Robert A. Sohn[1]

[1] Department of Geology and Geophysics, Woods Hole Oceanographic Institution, Woods Hole, Massachusetts, USA.

[2] Department of Geology and Geophysics, University of Hawaii, Manoa, Hawaii, USA.

[3] Research and Development Center for Earthquake and Tsunami, Japan Agency for Marine-Earth Science and Technology, Yokohama, Kanagawa, Japan.

OVERVIEW

This supplementary document contains additional information and images about the geophysical dataset, tomography modeling and checkerboard tests, MCS processing and interpretation, and details about calculations of the energy balance of the Rainbow hydrothermal field.

METHODS

Geophysical Dataset

The geophysical data were collected in April-May 2013 during the MARINER (Mid-Atlantic Ridge INtegrated Experiments at Rainbow) expedition onboard the *R/V Marcus G. Langseth* (cruise MGL1305). The experiment is centered on the Rainbow massif and extends 80 km in the ridge-parallel direction and 32 km across the ridge (Canales et al., 2013). The geophysical survey of the Rainbow area consisted of: (1) A large-scale 3D active-source seismic tomography experiment using 46 ocean bottom

seismometers (OBSs) and airgun sources. (2) Twenty-one 2D multichannel seismic (MCS) reflection profiles using one 8-km-long hydrophone streamer and airgun sources. (3) An ~8-month-long deployment of a network of 15 OBSs for long-term monitoring of the microseismicity of the Rainbow Massif and NTD. Analysis of this dataset is underway (Horning et al., 2015) and will be reported somewhere else. (4) Multibeam bathymetry and backscatter echosounding data, and underway potential fields (gravity and magnetics). These data and results from their analysis are reported in (Eason et al., 2016; Paulatto et al., 2015).

Three-Dimensional Traveltime Tomography From Wide-Angle Seismic Data

For three-dimensional (3D) refraction tomography, OBSs were placed within the study area with an average spacing of 7 km, but with increasing density toward the Rainbow massif (Fig. 1). A total of 46 OBSs were deployed and 43 provided full data sets. Each OBS contained a hydrophone and a 1- or 3-component geophone, and recorded at a sampling rate of 200 Hz. Approximately 3,800 airgun pulses were recorded by the OBS that were spaced every ~450 m along 26 seismic lines (Fig. 1). In addition, the airgun pulses of 21 MCS seismic lines (nominal source spacing of 37.5 m) were recorded by the inner 20 OBSs of the array. Seismic tomographic imaging was carried out using P-wave travel time data (~152,000 measurements) from both sets of seismic lines and an iterative technique that computes 3D velocity structure (Dunn, 2015; Dunn et al., 2005). Model parameters for isotropic velocity were spaced 0.5 km apart laterally, and vertically increased from 0.25 km at the seafloor to 1 km at 10 km depth; model parameters for azimuthal anisotropy were spaced 1 km laterally and increased from 0.5 km to 1 km from seafloor to 10 km depth. We constructed a 1D depth-varying starting model of P wave

velocities by laterally averaging the *Vp* model of (Dunn et al., 2005) for a nearby segment of the MAR. Then to obtain a stable 1-D starting model for the Rainbow area, we inverted all of the data using this starting model and solved for a 3D solution. The 3D anisotropic solution was then laterally averaged to create a new anisotropic 1D model, which was used as a starting model for a new 3D calculation. Several iterations were performed until the change in the 1D model from iteration-to-iteration was not significant. A grid search was performed by varying the strength of separate horizontal and vertical smoothness constraints on the tomographic image, to determine an acceptable range of 3D solutions that fit the data. Solutions with large smoothing values fit the data poorly. Very rough solutions also exhibit large data misfits and their velocity structures are too rough to be constrained by the data on the basis of the Fresnel zone of the seismic waves and checkerboard resolution tests. Models that best fit the data (chi-squared misfit ~1.0) occur over a small range of smoothness values and are very similar in appearance. Figure DR1 shows results of checkerboard resolution tests for vertical tomographic slices that pass through the Rainbow massif.

Two-Dimensional Multichannel Seismic Reflection Imaging.

Two-dimensional multichannel seismic (MCS) reflection data were collected across and along the Rainbow NTD and neighboring segments, comprising: seven NE-SW-oriented profiles ~82-97 km in length (Lines 101-107), six WNW-ESE-oriented profiles ~42-57 km in length (Lines 108, 110, 112, 114, 116, 118), six NW-SE-oriented profiles ~42 km in length (Lines 109, 111, 113, 115, 117, 119), and two auxiliary short profiles (Lines 122, 123) (Figs. 1, 2).

Acquisition parameters are given in Table DR1. MCS data processing consisted of 3 main stages: (1) processing of shot gathers to prepare the data for depth imaging, (2) pre-stack depth migration (PSDM) using as velocity model the long-wavelength *Vp* structure from the regional 3D tomography volume described above; and (3) post-migration image filtering and enhancement of low-frequency, laterally continuous reflectors for interpretation and display purposes. Detailed processing steps are listed in Table DR2. Figures DR2 and DR3 show the velocity model and pre- and post-enhancement PSDM images for two representative profiles (110 and 112, respectively).

Sill Identification, Picking, and Influence on Background *Vp*

Sill identification was done visually on each of the reflection sections. Reflectors within the Rainbow massif that have higher amplitudes than the background reflectivity, have waveforms characterized by a single or multiple peak-trough pairs, and are sub-horizontal or dip at low angle were interpreted as sills. We avoided interpreting as sills pronounced "smiles" that could be artifacts due to migration of off-plane seafloor scattering. Some of our interpreted sills have a moderate "smile" shape, which could be due to overmigration because of uncertainties in the velocity model, or a true geological shape, as concave-up or saucer-shaped magmatic sills are common in a variety of geological settings (e.g., Schofield et al., 2010; Thomson, 2007).

Picking of the sills was done using an automatic event-tracking algorithm following the negative (trough) amplitude of the waveform. Complex waveforms with multiple peak-trough pairs were interpreted as arising from multiple, closely stacked sills (e.g., Arnulf et al., 2014), and consequently stacked troughs were picked and assigned to

different sills. Figure DR4 shows an example of the interpretation and picking of sills along Line 112.

The presence of low-velocity sills should decrease the background *Vp* of the medium derived from the OBS data. We quantify this effect by using effective medium theory (Kuster and Toksöz, 1974). If the background medium is unaltered peridotite (*Vp*=8 km/s, Vs=4.5 km/s, density=3300 kg/m^3), and the sills are fully molten basalt (*Vp*=3.4 km/s, Vs=0 km/s, density=2.7 kg/m^3), 2% porosity (volume of sills relative to volume of material with *Vp*>7.3 km/s beneath the massif and above 8 km bsf) with aspect ratio (thickness/length) of 0.1 (as gabbroic sills in the Oman ophiolite Moho transition zone (Kelemen and Aharonov, 1998; Korenaga and Kelemen, 1997)) would produce an effective background *Vp* of 7.8 km/s. In the end-member case in which all of the sills are fully solidified gabbroic material (*Vp*=7 km/s, Vs=3.9 km/s, density=2900 kg/m^3), the effective background *Vp* is 7.98 km/s, basically indistinguishable from unaltered peridotite.

Therefore, if all of the sills where completely molten, some of the velocities in the core of the massif where the sills are emplaced (*Vp*=7.5-8.0 km/s) could be due to the effect of the low-velocity sills and not serpentinization, as indicated in Fig. 4D. In this case, the sills would be intruding even less altered peridotite (<10% serpentinized), strengthening our conclusion that the vast majority of the sills are emplaced in mantle material. We find the scenario in which all of the imaged sills are completely molten unlikely because of the minor presence of basalts on the surface of the massif (Andreani et al., 2014), and because even in magmatically robust mid-ocean ridges like the East

112 Pacific Rise, only small portions of the axial melt lens contain large amounts of melts
113 (Marjanović et al., 2015; Singh et al., 1998; Xu et al., 2014).

114 **Energy Calculations**

115 Parameters for the following calculations are given in Table DR3. The energy per
116 unit volume released by full crystallization of magma sills as they cool from the liquidus
117 (T_L) to the solidus temperature (T_S) is (Lowell, 2010):

118 $$U_m = \rho_m c_m \left(T_L - T_S\right) + \rho_m L$$

119 By computing the integrated volume of melt that all of the imaged sills could have stored
120 (V_m=4.9-9.2×10^9 m^3, for a range of sill thicknesses of 80-150 m (Benn et al., 1988;
121 Boudier et al., 1996; Kelemen and Aharonov, 1998; Korenaga and Kelemen, 1997; Xu et
122 al., 2014) and a circular plan-view geometry), we calculate the total energy released by
123 crystallization of the sills E_m = 1.52-2.86×10^{19} *J*.

124 We consider that the heat flux of the Rainbow hydrothermal system H=0.5 *GW*
125 (German et al., 2010) consists of three primary components (Lowell, 2010): heat
126 transported by mantle upwelling (H_M), heat produced by serpentinization (H_{serp}), and heat
127 released by cooling of magmatic intrusions (H_m). The heat flux per unit area transported
128 by mantle upwelling at a slow-spreading ridge is estimated to be 1.8 *MW km*$^{-2}$ (Lowell,
129 2010), which for Rainbow yields a mantle heat flux H_M=0.186 *GW*, or 37% of the
130 estimated total heat flux H. To calculate H_{serp} we first make an estimation of the volume
131 and mass of serpentinite in the Rainbow massif based on the 3D *Vp* model. For velocity
132 values between 5.0 and 7.9 km/s, we convert *Vp* to serpentine fraction (ϕ_{serp}) using the
133 relation (Miller and Christensen, 1997):

134 $$\phi_{serp} = \frac{7.95 - Vp[km/s]}{2.88}$$

135 *Vp* values >7.9 km/s are assumed to correspond to no serpentinization (ϕ_{serp}=0), while *Vp*
136 values <5.1 km/s are assumed to correspond to fully serpentinized material (ϕ_{serp}=1) in
137 which *Vp* is further decreased due to large-scale porosity and fracturing. This yields a
138 volume of serpentine of 277.2-281.5 km^3, corresponding to a mass of serpentine of 6.96-
139 7.07×10^{14} kg. The energy released by serpentinization is 2.5×10^5 $J\,kg^{-1}$ (Fyfe and
140 Lonsdale, 1981; Lowell, 2010), which yields an energy from serpentinization at Rainbow
141 of E_{serp}=1.74-1.77×10^{20} *J*, about 1.5 times of that estimated for the serpentinized Atlantis
142 Massif (Früh-Green et al., 2003). Assuming that the massif has been being uplifted and
143 serpentinized during the last 390,000 years, based on its location relative to the Brunhes-
144 Matuyama magnetic reversal (Paulatto et al., 2015), we estimate a heat flux due to
145 serpentinization of H_{serp}=0.014 *GW*, or 3% of the estimated total heat flux *H*. From H_{serp}
146 and H_M we then estimate that ~60% of the total heat flux *H*, or H_m=0.3 *GW*, at Rainbow
147 has a magmatic origin. From E_m and H_m we then estimate that the cumulative duration of
148 magmatic intrusions at Rainbow capable of sustaining high-temperature hydrothermal
149 activity is 1,613-3,022 years (Table DR3). This duration represents ~7–30% of the total
150 span of hydrothermal activity at Rainbow, which has been estimated to be between
151 10,000–23,000 years (Cave et al., 2002; Kuznetsov et al., 2006).

152 The above calculation does not account for the possibility of additional heat
153 provided by crystallization of melt impregnating peridotites, which is observed in mantle
154 rock samples from the MAR (Cannat et al., 1997; Takazawa et al., 2007). We repeat the
155 above calculations taking into account the heat released by crystallization of melt
156 impregnating peridotites. We assume that the proportion of this additional melt is 1-3%

of the volume of the massif because 1-3% is the proportion of seismically imaged sills relative to the volume of fresh-to-slightly altered mantle material (*Vp*>7.3 km/s). Factoring this additional melt, we find that magmatism at Rainbow could sustain high-temperature hydrothermal activity during 3,176-5,951 years (Table DR3), which is ~14-60% of system life.

Table DR1. MCS Acquisition Parameters During Cruise MGL1305	
Vessel	*RV Marcus G. Langseth*
Hydrophone streamer	Length: 8,000 m Number of groups: 636 Group spacing: 12.5 m Source to near channel: 210 m Cable depth: 12 m
Sources	Number: 1 Number of sub-arrays: 4 Number of guns per sub-array: 9 Total volume: 108 L (6,600 in^3) Pressure: 137.9 bar (2000 psi) Source interval: 37.5 m Source depth: 12 m
Recording	Sampling interval: 2 ms Record length: 12 s Format: SEG-D

169

170

Table DR2. MCS processing and depth imaging sequences
Pre-migration data preparation – Conversion to SEG-Y format – Geometry definition – Despiking using the LIFT method (Choo et al., 2004) using a procedure similar to those described in (Aghaei et al., 2014; Han et al., 2016): o Band-pass filtering: 1-6-100-125 Hz. o Resampling at 4 ms. o Separation of the wavefield in 3 frequency bands: low-pass filtered (15-20 Hz), high-pass filtered (20-25 Hz), and intermediate band by subtracting the low and high frequency components form the raw data. o One-pass (i.e., without the signal-add-back step) despiking and *f-k* filtering of the low-frequency component. o Two-pass despiking (i.e., with residual signal extracted from the noise component and added back after additional despiking) of the intermediate- and high-frequency components. o Summation of the 3 despiked frequency components to form cleaned shot gathers. – Spherical divergence correction. – Surface-consistent amplitude balancing. – Deconvolution of source signature. – Sorting in common-mid-point (CMP) gathers. – Bottom mute starting just above the primary sea-surface multiple.
Pre-stack depth migration – Definition of velocity model: o Extract *Vp* from the 3D isotropic regional tomography volume along the CMP locations. o Apply anisotropy correction based on the profile azimuth. o Resample at 5 m in depth. – Decomposition of the wavefield in plane waves and depth imaging using a wave-equation, finite-difference *f-x* pre-stack migration of each plane wave (Sourabas, 1996).
Post-migration image enhancement – Long-wavelength-pass filter (200-83 m). – *f-k* enhancement of flat or dipping events. – Laterally running mean filter. – Depth-dependent gain.

171

172

173

Table DR3. Parameters used in, and results of energy calculations			
Symbol	*Definition*	*Value*	*Reference*
	Age of Rainbow massif	390,000 yr	(Paulatto et al., 2015)
	Duration of hydrothermal activity	10,000-23,000 yr	(Cave et al., 2002; Kuznetsov et al., 2006)
	Duration of sill solidification-driven high-T hydrothermal activity	[(a)] 1,613-3,022 yr [(b)] 3,176-5,951 yr	This study
	Area covered by Rainbow massif	103.23 km^2	This study
	Sill thickness	80-150 m	(Boudier et al., 1996; Kelemen and Aharonov, 1998; Korenaga and Kelemen, 1997; Xu et al., 2014)
V_m	Volume of seismically imaged magma sills	4.9-9.2×10^9 m^3	This study
ρ_m	Density of magma	2700 kg m^{-3}	(Hooft and Detrick, 1993)
	Density of serpentine	2510 kg m^{-3}	(Miller and Christensen, 1997)
H	Heat flux through high-T fluids	0.5 GW	(German et al., 2010)
H_M	Heat flux from mantle upwelling	0.186 GW	This study
H_m	Heat flux from magma crystallization	0.300 GW	This study
H_{serp}	Heat flux from serpentinization	0.014 GW	This study
U_m	Energy per unit volume released by cooling of magma	3.12×10^9 J m^{-3}	This study
E_m	Energy released by cooling of magma	[(a)] 1.52-2.86×10^{19} J [(b)] 3.00-5.63×10^{19} J	This study
E_{serp}	Energy released by serpentinization	1.74-1.77×10^{20} J	This study
c_m	Specific heat of basaltic magma	1400 J kg^{-1} K^{-1}	(Liu and Lowell, 2011)
T_L	Liquidus temperature	1200 °C	(Lowell, 2010)
T_S	Solidus temperature	860 °C	(Coogan et al., 2001)
L	Latent heat of crystallization	6.8×10^5 J kg^{-1}	(Fukuyama, 1985)
[(a)] Assuming no additional melt impregnating peridotites. [(b)] Assuming 1-3% of additional melt impregnating peridotites.			

174

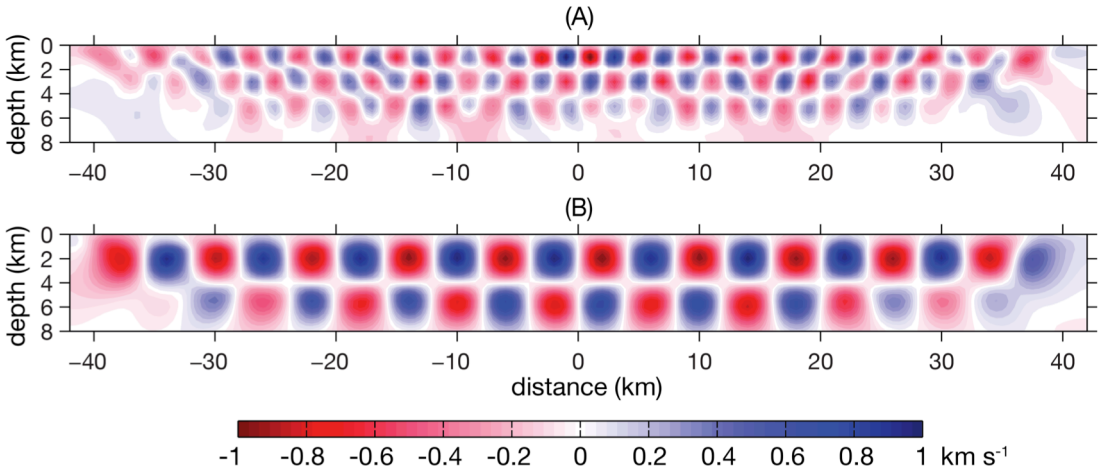

Fig. DR1. Checkerboard reconstructions illustrating the resolving power of the tomography experiment. The reconstructions used the same ray paths, matrix of partial derivatives (weighted by data uncertainties), and regularization constraints as for the solution shown in the main text. The result is shown for the first iteration of the forward and inverse problem; subsequent iterations improve the magnitudes of the checkers, but not their form. Vertical cross sections are shown for locations along the centerline of the long-axis of the experiment (SW-NEW direction, Fig. 1) for **(A)**, 2x2x2 km^3 and **(B),** 4x4x4 km^3 size anomalies. Overall, the best resolution occurs within the station bounds and above 8 km depth. Target checkerboard tests with the depth range of 8-10 km (not shown), where only ~2000 rays sample in total, found only large scale features can be detected (>10 km), but not without significant smearing and distortion. The Rainbow hydrothermal field is located at 0 km distance along the horizontal axis.

175

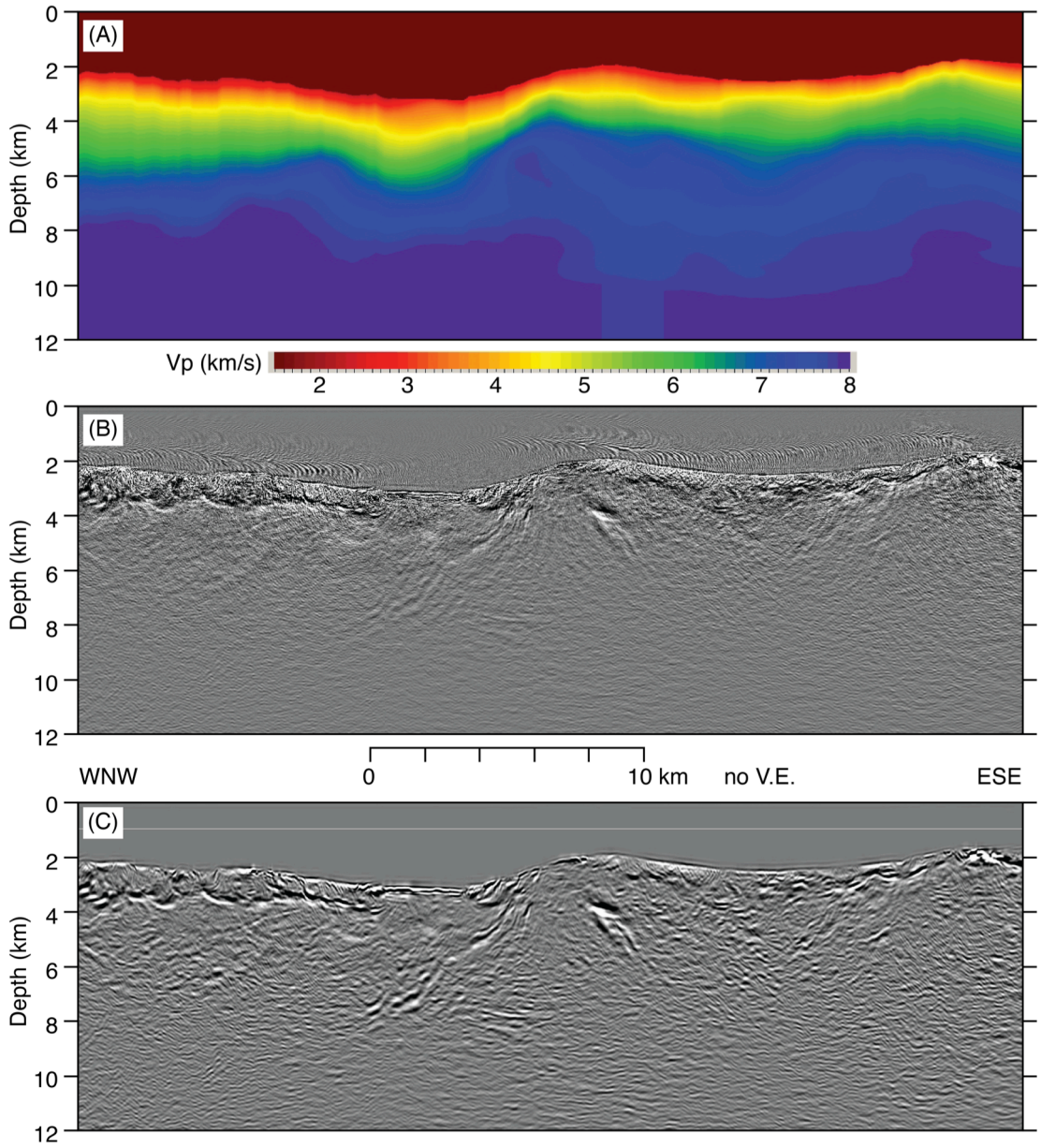

Fig. DR2. (A) Velocity model used for PSDM of Line 110. **(B)** PSDM image of Line 110. **(C)** Filtered and enhanced PSDM image of Line 110.

176

177

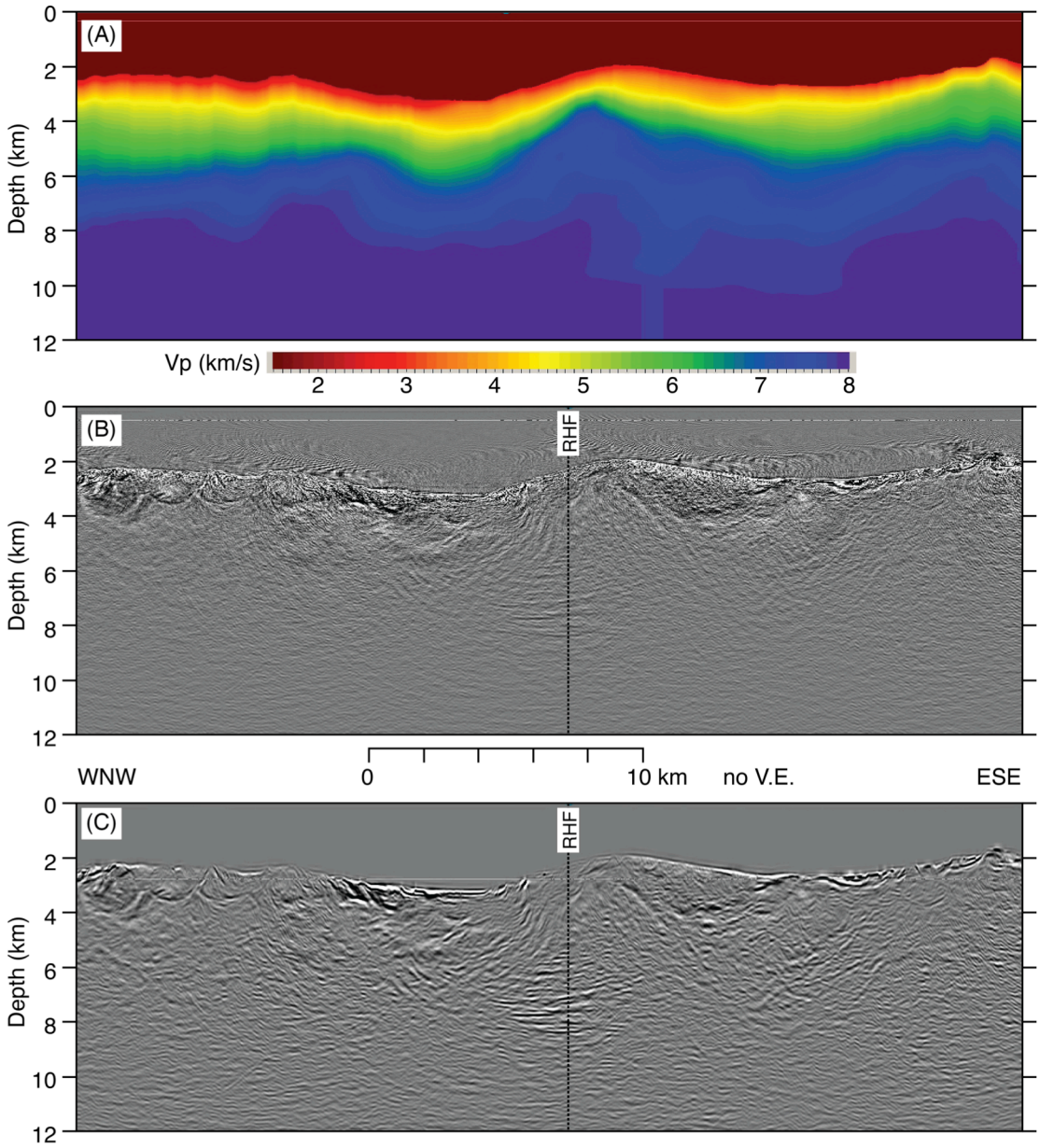

Fig. DR3. Same as Fig. DR2 for Line 112. RHF: Rainbow hydrothermal field.

178

179

180

181

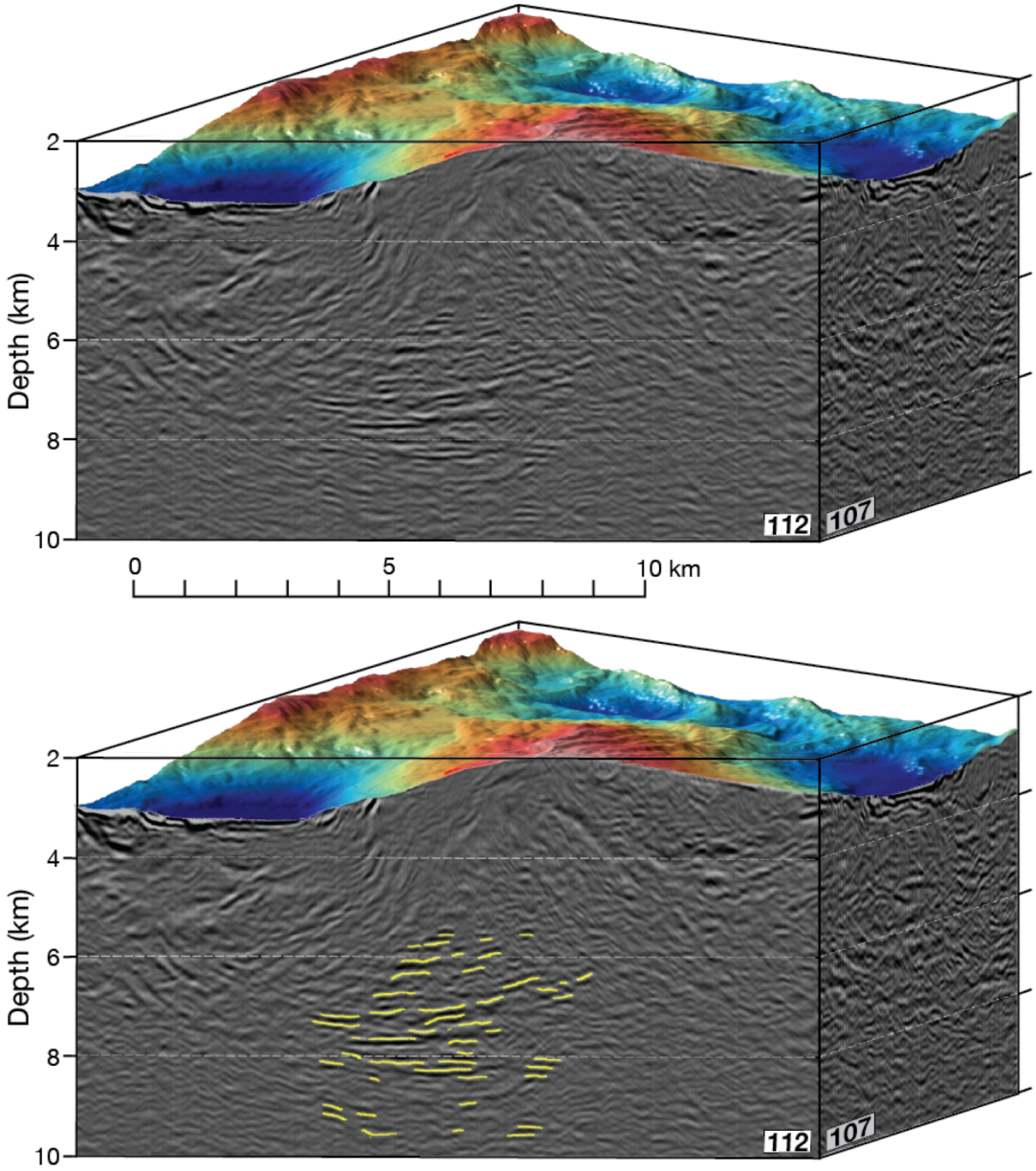

Fig. DR4. Portion of MCS reflection profile Line 112 illustrating the identification and picking of reflectors interpreted as sills (yellow lines in bottom panel).

182

183

184 **Supplementary References**

185 Aghaei, O., Nedimović, M. R., Carton, H., Carbotte, S. M., Canales, J. P., and Mutter, J.
186 C., 2014, Crustal thickness and Moho character of the fast-spreading East Pacific
187 Rise from 9˚42'N to 9˚57'N from poststack-migrated 3D MCS data:
188 Geochemistry, Geophysics, Geosystems, v. 15, p. doi: 10.1002/2013GC005069.
189 Andreani, M., Escartín, J., Delacour, A., Ildefonse, B., Godard, M., Dyment, J., Fallick,
190 A. E., and Fouquet, Y., 2014, Tectonic structure, lithology, and hydrothermal
191 signature of the Rainbow massif (Mid-Atlantic Ridge 36^{o}14'N): Geochemistry,
192 Geophysics, Geosystems, v. 15, p. doi:10.1002/2014GC005269.
193 Arnulf, A. F., Singh, S. C., and Pye, J. W., 2014, Seismic evidence of a complex multi-
194 lens melt reservoir beneath the 9^{o}N overlapping spreading center at the East
195 Pacific Rise: Geophysical Research Letters, v. 41, p. doi:10.1002/2014GL060859.
196 Benn, K., Nicolas, A., and Reuber, I., 1988, Mantle-crust transition zone and origin of
197 wehrlitic magmas: Evidence from the Oman ophiolite: Tectonophysics, v. 15, p.
198 75-85.
199 Boudier, F., Nicolas, A., and Ildefonse, B., 1996, Magma chambers in the Oman
200 ophiolite: fed from the top and the bottom: Earth and Planetary Science Letters, v.
201 144, p. 239-250.
202 Canales, J. P., Dunn, R. A., Swift, S. A., Paulatto, M., Arai, R., Szitkar, F., Horning, G.,
203 Fabeta, M., Benazzouz, O., Kakone, E., Griesche, H., McHugh, C., and Sohn, R.
204 A., 2013, MARINER: Seismic Investigation of the Rainbow Hydrothermal Field
205 and its Tectono/Magmatic Setting, Mid-Atlantic Ridge 36^{o}14'N- A Report from
206 RV M.G. Langseth Cruise MGL1305: InterRidge News, v. 22, p. 43-50.
207 Cannat, M., Chatin, F., Whitechurch, H., and Ceuleneer, G., 1997, Gabbroic rocks
208 trapped in the upper mantle at the mid-Atlantic ridge, *in* Karson, J. A., Cannat,
209 M., Miller, D. J., and Elthon, D., eds., Proceedings of the Ocean Drilling Program
210 Scientific Results, Volume 153, ODP, p. 243-264.
211 Cave, R. R., German, C. R., Thomson, J., and Nesbitt, R. W., 2002, Fluxes to sediments
212 underlying the Rainbow hydrothermal plume at 36°14'N on the Mid-Atlantic
213 Ridge: Geochimica et Cosmochimica Acta, v. 66, no. 11, p. 1905-1923.
214 Choo, J., Downton, J., and Dewar, J., 2004, Lift: A new and practical approach to noise
215 and multiple attenuation: First Break, v. 22, p. 39-44.
216 Coogan, L. A., Wilson, R. N., Gillis, K. M., and MacLeod, C. J., 2001, Near-solidus
217 evolution of oceanic gabbros: Insights from amphibole geochemistry: Geochimica
218 et Cosmochimica Acta, v. 65, no. 23, p. 4339-4357.
219 Dunn, R. A., 2015, Tracking stress and hydrothermal activity along the Eastern Lau
220 Spreading Center using seismic anisotropy: Earth and Planetary Science Letters,
221 v. 410, p. 105-116.
222 Dunn, R. A., Lekic, V., Detrick, R. S., and Toomey, D. R., 2005, Three-dimensional
223 seismic structure of the Mid-Atlantic Ridge (35°N): Evidence for focused melt
224 supply and lower crustal dike injection: Journal of Geophysical Research, v. 110,
225 p. B09101.

Eason, D. E., Dunn, R. A., Canales, J. P., and Sohn, R., 2016, Segment-scale variations in seafloor volcanic and tectonic processes from multibeam sonar imaging, Mid-Atlantic Ridge Rainbow region (35º45'-36º35'N): Geochemistry, Geophysics, Geosystems, v. 17, p. doi:10.1002/2016GC006433.

Früh-Green, G. L., Kelley, D. S., Bernasconi, S. M., Karson, J. A., Ludwig, K. A., Butterfield, D. A., Boschi, C., and Proskurowski, G., 2003, 30,000 years of hydrothermal activity at the Lost City vent field: Science, v. 301, p. 495-498.

Fukuyama, H., 1985, Heat of fusion of basaltic magma: Earth and Planetary Science Letters, v. 73, p. 407-414.

Fyfe, W. S., and Lonsdale, P., 1981, Ocean Floor Hydrothermal Activity, *in* Emiliani, C., ed., The Sea, Volume 7: New York, Wiley & sons, p. 589-638.

German, C. R., Thurnherr, A. M., Knoery, J., Charlou, J.-L., Jean Baptiste, P., and Edmonds, H. N., 2010, Heat, volume and chemical fluxes from submarine venting: A synthesis of results from the Rainbow hydrothermal field, 36^{o}N MAR: Deep Sea Research Part I, v. 57, p. 518-527.

Han, S., Carbotte, S. M., Canales, J. P., Carton, H., Nedimović, M. R., Gibson, J., and Horning, G., 2016, Seismic reflection imaging of the Juan de Fuca plate from ridge to trench; new constraints on the distribution of faulting and evolution of the crust prior to subduction: Journal of Geophysical Research, v. 121, p. doi:10.1002/2015JB012416.

Hooft, E., and Detrick, R. S., 1993, The role of density in the accumulation of basaltic melts at mid-ocean ridges: Geophysical Research Letters, v. 20, no. 6, p. 423-426.

Horning, G., Canales, J. P., Sohn, R., and Dunn, R. A., 2015, Analysis of microearthquakes at the non-transform offset of the Mid-Atlantic Ridge hosting the Rainbow hydrothermal system (36^{o}14'N): Abstract OS43A-2000 presented at 2015 Fall Meeting, AGU, San Francisco, Calif., 14-18 Dec.

Kelemen, P. B., and Aharonov, E., 1998, Periodic formation of magma fractures and generation of layered gabbros in the lower crust beneath oceanic spreading ridges, *in* Buck, W. R., Delaney, P. T., Karson, J. A., and Lagabrielle, Y., eds., Faulting and Magmatism at Mid-Ocean Ridges, Volume 106: Washington, D.C., AGU, p. 267-289.

Korenaga, J., and Kelemen, P. B., 1997, Origin of gabbro sills in the Moho transition zone of the Oman ophiolite: Implications for magma transport in the oceanic lower crust: Journal of Geophysical Research, v. 102, p. 27,729-727,749.

Kuster, G. T., and Toksöz, M. N., 1974, Velocity and attenuation of seismic waves in two-phase media: Part I. Theoretical formulations: Geophysics, v. 39, no. 5, p. 587-606.

Kuznetsov, V., Cherkashev, G., Lein, A., Shilov, V., Maksimov, F., Arslanov, K., Stepanova, T., Baranova, N., Chernov, S., and Tarasenko, D., 2006, ^{230}Th/U dating of massive sulfides from the Logatchev and Rainbow hydrothermal fields (Mid-Atlantic Ridge): Geochronometria, v. 25, p. 51-55.

Liu, L., and Lowell, R. P., 2011, Modeling heat transfer from a convecting, crystallizing, replenished silicic magma chamber at an oceanic spreading center: Geochemistry, Geophysics, Geosystems, v. 12, no. 9, p. Q09010.

Lowell, R. P., 2010, Hydrothermal circulation at slow spreading ridges: Analysis of heat sources and heat transfer processes, *in* Rona, P., Devey, C. W., Dyment, J., and

Murton, B., eds., Diversity of Hydrothermal Systems on Slow Spreading Ocean Ridges: Washington, D.C., AGU, p. 11-26.

Marjanović, M., Carton, H., Carbotte, S. M., Nedimović, M. R., Mutter, J. C., and Canales, J. P., 2015, Distribution of melt along the East Pacific Rise from 9o30' to 10oN from an amplitude variation with angle of incidence (AVA) technique: Geophysical Journal International, v. 203, p. 1-21.

Miller, D. J., and Christensen, N. I., 1997, Seismic velocities of lower crustal and upper mantle rocks from the slow spreading Mid-Atlantic Ridge, south of the Kane transform zone (MARK), *in* Karson, J. A., Cannat, M., Miller, D. J., and Elthon, D., eds., Proceedings of the Ocean Drilling Program Scientific Results, Volume 153: College Station, TX (Ocean Drilling Program), p. 437-454.

Paulatto, M., Canales, J. P., Dunn, R. A., and Sohn, R. A., 2015, Heterogeneous and asymmetric crustal accretion: new constraints from multi-beam bathymetry and potential field data from the Rainbow area of the Mid-Atlantic Ridge (36°15'N): Geochemistry, Geophysics, Geosystems, v. 16, p. doi:10.1002/2105GC005743.

Schofield, N., Stevenson, C., and Reston, T., 2010, Magma fingers and host rock fluidization in the emplacement of sills: Geology, v. 38, no. 1, p. 63-66.

Singh, S. C., Kent, G. M., Collier, J. S., Harding, A. J., and Orcutt, J. A., 1998, Melt to mush variations in crustal magma properties along the ridge crest at the southern East Pacific Rise: Nature, v. 394, p. 874-878.

Sourabas, R., 1996, Explicit 3-D migration using equiripple polynomial expansion and Laplacian synthesis: Geophysics, v. 61, no. 5, p. 1386-1393.

Takazawa, E., Abe, N., Seyler, M., and Meurer, W. P., 2007, Hydridization of dunite and gabbroic materials in Hole 1271B from Mid-Atlantic Ridge 15^{o}N: Implications for melt flow and reaction in the upper mantle, *in* Kelemen, P., Kikawa, E., and Miller, D. J., eds., Proceedings of the Ocean Drilling Program Scientific Results, Volume 209: College Station, TX (Ocean Drilling Program), p. 1-24. doi:10.2973/opd.proc.sr.2209.2005.2007.

Thomson, K., 2007, Determining magma flow in sills, dykes and laccoliths and their implications for sill emplacement mechanisms: Bulletin of Volcanology, v. 70, p. 183-201.

Xu, M., Canales, J. P., Carbotte, S. M., Carton, H., Nedimović, M. R., and Mutter, J. C., 2014, Variations in axial magma lens properties along the East Pacific Rise (9°30'-10°00'N) from swath 3D seismic imaging and 1D waveform inversion: Journal of Geophysical Research, v. 119, p. doi:10.1002/2013JB010730.